J. Fluid Mech. (2006), *vol.* 558, *pp.* 357–386.
doi:10.1017/S0022112006000061 Printed in the United Kingdom

On Boussinesq and non-Boussinesq starting forced plumes

By JIAOJIAN AI[1], ADRIAN WING-KEUNG LAW[2] AND S. C. M. YU[1]

[1]School of Mechanical and Aerospace Engineering, Nanyang Technological University, Singapore 639798

[2]School of Civil and Environmental Engineering, Nanyang Technological University, Singapore 639798

(Received 5 August 2005 and in revised form 14 November 2005)

The characteristics of Boussinesq and non-Boussinesq starting forced plumes were investigated in this study. Two distinct periods in the transient plume penetration are identified, namely, the period of flow development (PFD) and period of developed flow (PDF). Similarity solutions are developed in PDF by incorporating the behaviour of an isolated buoyant vortex ring and recent laboratory results on the trailing forced plume, and the temporal variation of the penetration rate is derived during the different phases of jet-like, transitional and plume-like flow. To verify the similarity solutions, experiments were conducted on vertical starting forced plumes using combined particle image velocimetry (PIV) and planar laser induced fluorescence (PLIF) with refractive index matching. The discharge Reynolds number was varied from 3773 to 7403 and the range of excess densities ($\Delta_0 = (\rho_\infty - \rho_0)/\rho_\infty$, where ρ_0 and ρ_∞ are initial plume and ambient density, respectively) from 2.77 % to 25.07 %. The experimental results revealed distinct differences between plumes having an initial density difference of larger or smaller than 15 % due to the non-Boussinesq effects. Thus, the value of 15 % was employed as an approximate criterion to divide the plumes into Boussinesq versus non-Boussinesq cases. The measured penetration rates and the mean centreline axial velocity of the Boussinesq starting forced plumes agreed well with the analytical predictions at the fully developed stage. However, the behaviour was substantially more complex for the non-Boussinesq plumes. In the transient records, it was noted that the time scales for the penetration of the starting plumes and the velocity development in the trailing forced plume were similar, but the time scale for the Gaussian profile to become self-similar was somewhat longer.

1. Introduction

Starting forced plumes are common phenomena with a wide spectrum of physical scales from the releases of hot ash during volcanic eruptions to the emission of chemical plumes by accidental or intentional releases in an indoor environment. Quantifying the mixing and entrainment of the starting forced plumes is thus of substantial engineering and environmental interests.

A forced plume, or buoyant jet, possesses both initial momentum and buoyancy fluxes. For a round port with a diameter D, an exit velocity W_0, an average initial density ρ_0 and a uniform ambient density ρ_∞, the source parameters, i.e. buoyancy,

Cases	W_0 (m s^{-1})	ρ_∞ (kg l^{-1})	ρ_0 (kg l^{-1})	Δ_0 (%)	R_e	L_m (mm)	Fr_0	Λ	Time interval between laser pulse pair (ms)
C1	0.503	1.0258	0.9974	2.77	3773	78.1	9.80	0.022	4
C2	0.503	1.0552	0.9974	5.48	3773	55.4	6.95	0.044	4
C3	0.987	1.0552	0.9974	5.48	7500	110.8	13.91	0.011	2
C4	0.503	1.1007	0.9974	9.38	3750	42.4	5.32	0.075	4
C5	0.987	1.1007	0.9974	9.38	7403	84.8	10.64	0.019	2
C6	0.503	1.1518	0.9974	13.40	3773	35.5	4.46	0.108	4
C7	0.987	1.1518	0.9974	13.40	7403	71.0	8.91	0.027	2
C8	0.503	1.0997	0.8857	19.45	3773	29.0	3.63	0.161	4
C9	0.987	1.0997	0.8857	19.45	7403	57.9	7.27	0.040	2
C10	0.503	1.1171	0.8370	25.07	3773	26.1	3.26	0.199	4
C11	0.987	1.1171	0.8370	25.07	7403	52.2	6.53	0.050	2

TABLE 1. Initial parameters of the experiments.

momentum and mass fluxes (B_0, M_0, Q_0), can be defined as,

$$B_0 = \tfrac{1}{4}\pi D^2 W_0 \frac{\rho_0 - \rho_\infty}{\rho_\infty} g = \frac{\rho_0 - \rho_\infty}{\rho_\infty} g Q_0 = g_0' Q_0, \tag{1a}$$

$$M_0 = \tfrac{1}{4}\pi D^2 W_0^2, \tag{1b}$$

$$Q_0 = \tfrac{1}{4}\pi D^2 W_0, \tag{1c}$$

where g denotes the acceleration due to gravity and $g_0' = g\Delta_0$ is the initial reduced gravity. A function of the dimensionless source parameters,

$$\Lambda = \frac{5 Q_0^2 B_0}{4\alpha M_0^{5/2}}, \tag{2}$$

where α represents the entrainment coefficient, can be used to categorize the buoyant plumes as suggested by Morton (1959). He defined the pure plumes as $\Lambda = 1$, the forced plumes to be those with an initial momentum flux greater than that of an equivalent pure plume of the same initial buoyancy flux (i.e. $0 < \Lambda < 1$), and lazy plumes as $\Lambda > 1$. The Λ values shown in table 1 indicate that the experiments conducted in the present study were all with forced plumes.

A starting forced plume is substantially more complex than a steady forced plume owing to the interaction between the head vortex and the trailing stem. Based on published work (e.g. Gharib, Rambod & Shariff 1998; Ai *et al.* 2005), we find that the temporal development of a starting forced plume can be separated into two distinct periods that can be termed the period of flow development (PFD) and period of developed flow (PDF), in analogy with the zone of flow establishment (ZFE) and zone of established flow (ZEF) that are well known for a steady jet (Crow & Champagne 1971; Fischer *et al.* 1979). PFD represents the initial period after the fluid ejection, when the exit conditions generate longitudinal and azimuthal vortices and their interactions lead to complex vortical dynamics near the source such as the occurrence of vortex coalescence and leapfrogging (Ai *et al.* 2005). When the circulation of the head vortex reaches its maximum, the head vortex may then detach from the trailing stem. The detachment is known as the pinch-off phenomenon (Gharib *et al.* 1998). Owing to the decay of the head vortex ring, the detached head vortex and the trailing forced stem would, however, reconnect after some time, at

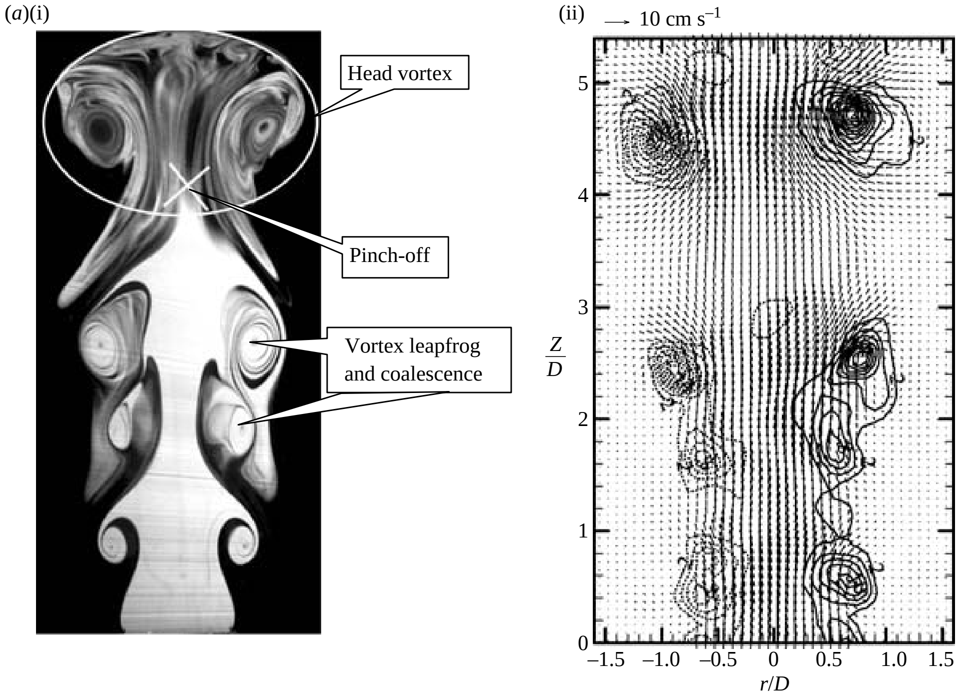

FIGURE 1. (*a*) A pictorial sketch of the vortical dynamics in PFD: (i) flow visualization by PLIF, and (ii) corresponding vector and vorticity map by PIV. The image was obtained in a starting jet experiment with $R_e = 4716$.

which point the PFD ends and the starting forced plume becomes fully developed, independent of the exit conditions. Here, the term ‘fully developed’ also implies that the characteristics of the plume become self-similar and can be evaluated by the similarity law. Noticeably, because of the pinch-off and reconnection, an overshoot in penetration is typically observed in PFD (Ai *et al.* 2005) which can be attributed to the initial acceleration due to over-pressure at the exit of the nozzle as the forced plume is initiated (see figure 7 for an illustration). Figure 1(*a*) shows a sketch of the pinch-off process in PFD.

The plume characteristics in PDF are relatively simpler and more predictable, because they depend primarily on the feeding of momentum and buoyancy fluxes into the head vortex by the trailing stem. Again, in analogy with the interplays between initial and buoyancy-induced momentum flux in a steady plume, a fully developed starting forced plume would also experience three phases of penetration behaviour during its vertical rise: jet-like, transitional and plume-like. Together with the head vortex formation and interaction phase in PFD, in which the asymptotic behaviour of the head vortex is significant, the four phases are depicted schematically in figure 1(*b*). Three regions, i.e. jet-like, transitional and plume-like, appear sequentially in the trailing stem. In the asymptotic jet-like and plume-like regions of the trailing stem, the starting forced plume is dominated by the initial momentum and buoyancy fluxes, respectively, and its behaviours are comparable to a starting pure jet and pure plume, respectively. Therefore, the flow in these two asymptotic regions can be deemed as a pure jet or plume arising from a virtual point source with zero mass flux. In the transitional region, however, the forced plume is influenced by both the initial momentum

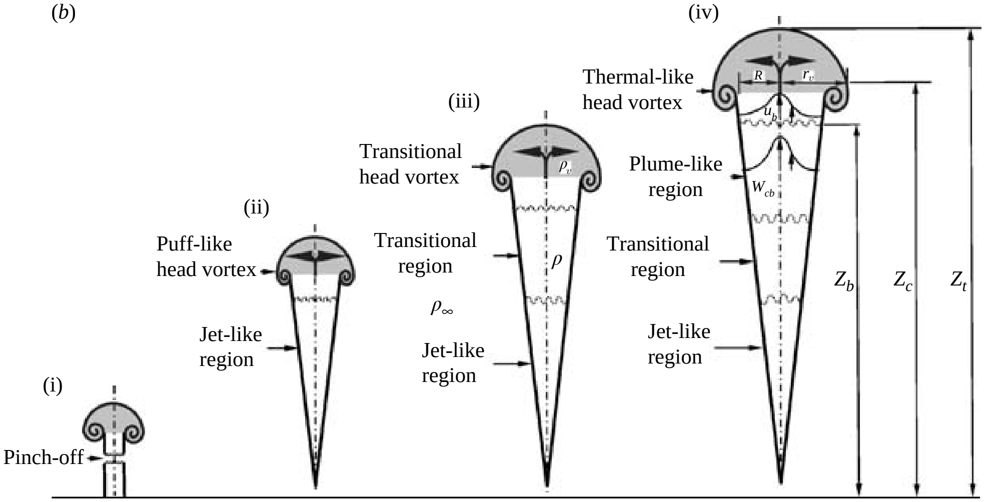

FIGURE 1. (*b*) Schematic diagram of the four different phases for the development of a starting plume. (i) Period of flow development. (ii)–(iv) Period of developed flow. (i) Vortex formation and interaction phase; (ii) jet-like phase; (iii) transitional phase; (iv) plume-like phase.

and buoyancy fluxes. The head vortex will also undergo four stages, namely, formation, puff-like, transitional and thermal-like. Note that, depending on the comparative strength of the initial buoyancy and momentum fluxes, the PFD of the starting forced plume can overwhelm the jet-like phase through the overshoot of the head vortex ring. Therefore, a fully developed starting forced plume may directly enter into the transitional and plume-like phase in PDF.

Previous experimental, theoretical and computational studies focus mostly on either starting pure jets or starting pure plumes. They include Turner (1962), Delichatsios (1979), Sangras & Faeth (1999), Pantzlaff & Lueptow (1999) and Diez, Sangras & Faeth (2003). For starting jets, it has been shown that the transient jet penetration velocity, u_t, is inversely proportional to the square root of time (Witze 1980; Johari, Zhang & Bourque 1997; Hill & Ouellette 1999; Cossali, Coghe & Araneo 2001; Ai *et al.* 2005). On the other hand, Middleton (1975) suggested that the starting plume penetration has a smaller time exponent of $-1/4$ based on Turner's (1962) model (i.e. $u_t \propto B_0^{1/4} t^{-1/4}$, where t is time). The $-1/4$ time behaviour for starting plumes is also supported by the recent analysis of Diez *et al.* (2003). Delichatsios (1979) further reported that the advancing velocity at the leading edge of the plume is less than the velocity in the plume interior with a maximum ratio of 0.42, although both bear the same temporal development.

There have been comparatively fewer studies on starting forced plumes. Plantzlaff & Lueptow (1999) reported that positively starting forced plumes have a similar dependence on time to the pure jets, at least in the momentum-dominated region. Diez *et al.* (2003) proposed a time scale $t^* = (D^4/B_0)^{1/3}$, and suggested that the penetration distance Z_t normalized by D is proportional to the time normalized by this time scale with a power of 3/4 (i.e. $(Z_t - Z_0)/D \sim (t/t^*)^{3/4}$, where Z_0 represents the virtual origin). By adopting the virtual origin for a bulk correction of the non-self-preserving behaviours, Diez *et al.* (2003) did not give a detailed description of the various developmental phases of the plume penetration as is done here.

The dynamics of a starting forced plume in PDF relates directly to the coupling behaviour between the head vortex and the trailing stem. Hence, the penetration characteristics of the starting forced plume can be predicted using the characteristics of isolated vortex rings and the trailing stem which can be related to the steady forced plume via a quasi-steady approximation (Heskestad 1972), in which the properties of the two are assumed to be similar.

In terms of the separate behaviour of the head vortex and the trailing stem, there is now substantial knowledge available in the recent literature. On the head vortex, much of the characteristics of momentum puffs and thermals (without and with buoyancy, respectively) are now known in a neutral surrounding (Turner 1957; Saffman 1975, 1978; Maxworthy 1977; Didden 1979; Pullin 1979; Glezer 1988; Lundgren & Mansour 1991). The comprehensive reviews of Shariff & Leonard (1992) and Lim & Nickels (1995) discussed the current understanding of vortex ring phenomena as well as some unresolved issues. For the trailing forced plume stem, steady-state Boussinesq characteristics have been investigated in great detail (e.g. Morton, Taylor & Turner 1956; Wyganski & Fiedler 1969; Fischer *et al.* 1979) and quantitative relationships for the velocity and scalar behaviour are now available with high accuracy (Papanicolaou & List 1988; Shabbir & George 1994; Wang & Law 2002).

A main objective of the present study is to develop a model for the fully developed period of a starting Boussinesq forced plume that extends from the asymptotic jet-like to the asymptotic plume-like phases. Such a detailed model is not available at present. Subsequently, experiments on starting forced plumes were conducted using combined particle image velocimetry (PIV) and planar laser induced fluorescence (PLIF) with refractive index matching. The scope of the experiments included a relative density difference, Δ_0, of up to 25.07 %, and thus covered cases of both Boussinesq and non-Boussinesq starting forced plumes. The experimental results and observations of the non-Boussinesq cases will be presented for the first time, and it will be shown that the plume behaviours are distinctly different in the higher density difference cases.

It should be noted that the published work on non-Boussinesq plumes is very limited. Rooney & Linden (1996) derived the theoretical form of entrainment velocity across the plume edge which had been postulated from the experimental observations by Ricou & Spalding (1961). Subsequently, their model was applied to different fire experiments in Rooney & Linden (1997) and Woods (1997). Zhou, Luo & Williams (2001) performed a detailed simulation on the non-Boussinesq plumes with two different large density ratios of 2.0 and 3.0.

In the following, we shall first review the current understanding on the behaviour of isolated vortex rings and forced plumes. Subsequently, their coupling dynamics for a starting forced plume are addressed.

2. Isolated vortex ring

Depending on the developmental phase, the cap of a starting forced plume can be considered as a vortex ring that is similar to a momentum puff (jet-like) or thermal (plume-like). A turbulent vortex ring or momentum puff being independent of Reynolds number can be described as a compact turbulent region that is statistically invariant with respect to the rotation about an axis in the azimuthal direction (Shariff & Leonard 1992). Helmholtz (1858) proposed a method for computing the translational speed of thin rings that depends weakly on σ/R (where σ and R are the characteristic ring core size and ring radius, respectively). The weak dependence can be ignored to provide an approximate speed for the motion of the vorticity centroid.

This approach was used by Kelvin (1880) to obtain the speed of a thin steady ring with uniform vorticity. The method is described as follows.

The momentum of all the fluid moving with a vortex ring that is approximated to be thin reads (Lamb 1932),

$$M_v = \pi \rho_v \Gamma R^2, \tag{3}$$

where Γ is the circulation, ρ_v is the mean density of the thermal or vortex ring and R the 'mean ring radius' defined by Lamb (1932) as (denoted in figure 1*b*(iii)),

$$R = \left(\frac{\displaystyle\int_0^\infty \int_0^\infty r^2 \omega \, \mathrm{d}r \, \mathrm{d}h}{\displaystyle\int_0^\infty \int_0^\infty \omega \, \mathrm{d}r \, \mathrm{d}h} \right)^{1/2}, \tag{4}$$

where r and h are the radial and vertical coordinates, respectively, and ω is the local vorticity. Assuming that the distribution of vorticity in the cap remains similar at all heights and that the ambient is not stratified so that zero net baroclinic vorticity is generated by the baroclinic torque, the velocity of the vortex centre, u_c, can be expressed as

$$u_c = C_1 \Gamma / R, \tag{5}$$

where C_1 is a constant. The value for C_1 should differ between a momentum puff and a thermal, although their order of magnitude is probably similar. It is convenient for the present purpose to eliminate Γ from (5) and (3) to give,

$$M_v = (\pi \rho_v / C_1) R^3 u_c. \tag{6}$$

Turner (1957) suggested that a thermal can be regarded as a special case of an isolated buoyant vortex ring, in which case the increase in momentum is solely due to the total buoyancy force F_v and the temporal change rate of the momentum can be expressed as

$$\frac{\mathrm{d}M_v}{\mathrm{d}t} = \rho_\infty F_v. \tag{7}$$

The laboratory experiments of Sangras & Faeth (1999) showed that a thermal consists of a region of turbulent buoyant fluid with its radius expanding linearly with distance as the thermal mixes with its surroundings. The addition of outside fluid takes place partly by mixing over the thermal front and partly by drawing up fluid from behind. In this sense, it can be said that a thermal leaves no wake behind.

Overall, we can consider the head vortex as a buoyant ring vortex that is growing by the turbulent entrainment of the external ambient fluid and the trailing forced plume.

3. Trailing forced plume

The starting forced plume possesses a trailing stem that with time would develop into a steady forced plume. Similarity solutions for steady forced plumes were first investigated by Morton *et al.* (1956), using conservation equations representing the mass, momentum and buoyancy fluxes (see Appendix). An important assumption in this approach is that the local variations in buoyancy are small, such that the profiles of mean vertical velocity and mean buoyancy are of similar form at all cross-sections within the plume (Turner 1969). The assumption is equivalent to the so-called Boussinesq assumption. The model provides a practical approach for the simulation of a forced plume, but it cannot be applied to analyse the exit region near the origin of the forced plume where the profiles are developing and not self-similar.

A detailed experimental investigation on the quantitative characteristics of a vertical forced plume, or buoyant jet, was performed by Wang & Law (2002) using combined PIV and PLIF. The investigation covered the three regions of a developed steady forced plume from jet-like, transitional to plume-like. Based on the experimental results, they reported that the decay of the centreline velocity W_c over the developed range is as follows:

$$\log\left(\frac{\sqrt{M_0}}{ZW_c}\right) = g(\xi), \tag{8a}$$

where Z is the axial coordinate and

$$\begin{aligned} g(\xi) = {} & -\tfrac{1}{3}[1+\tanh(k_1\xi-\eta_1)]\xi + \log\left(\frac{1}{k_{pw}}\right) \\ & + \tfrac{1}{2}\left[\log\left(\frac{1}{k_{pw}}\right) - \log\left(\frac{\sqrt{\pi}}{2k_{jw}}\right)\right][\tanh(k_2\xi-\eta_2)-1] - k_4\exp[-k_3(\xi-\eta_3)^2], \end{aligned} \tag{8b}$$

$$\xi = \log\left(\frac{Z}{L_m}\right), \tag{8c}$$

where L_m is the momentum length scale which is defined as (Morton 1959; List 1982):

$$L_m = \frac{M_0^{3/4}}{B_0^{1/2}}. \tag{9}$$

L_m is pertinent to buoyant flows and measures the distance required for the buoyancy-induced momentum to dominate over the momentum of the source flow.

The constants in (8*b*) were determined by the experiments in Wang & Law (2002) as: $k_1 = 3.110$, $k_2 = 2.815$, $k_3 = 6.123$, $k_4 = 0.0797$, $\eta_1 = 1.831$, $\eta_2 = 2.067$, $\eta_3 = 0.4529$, $k_{jw} = 6.477$ and $k_{pw} = 4.13$. These constants define quantitatively the self-similar behaviour of the centreline velocity for the different stages of a forced plume. Equation (8*a*) automatically contains the jet-like and plume-like regions. As $\xi \to -\infty$, (8*b*) reduces to:

$$g(\xi) = \log\left(\frac{\sqrt{\pi}}{2k_{jw}}\right), \tag{10}$$

which is equivalent to the well-known equation for pure jets (Fischer *et al.* 1979), i.e.

$$W_c = k_{jw} W_0 (Z/D)^{-1}. \tag{11}$$

As $\xi \to +\infty$ and (8*b*) becomes:

$$g(\xi) = -\tfrac{2}{3}\xi + \log\left(\frac{1}{k_{pw}}\right), \tag{12}$$

which is identical to the asymptotic behaviour for the centreline velocity of a pure plume (Fischer *et al.* 1979), i.e.

$$W_c = k_{pw} B_0^{1/3} Z^{-1/3}. \tag{13}$$

4. Penetration rate of a starting forced plume

In this section, we shall develop a model for the penetration rate of a starting forced plume that spans the entire developed range by quantifying the linkage between the head vortex and the trailing forced plume stem.

As mentioned previously, the original and pioneering conceptualization should be attributed to Turner (1962) who proposed that a starting plume can be modelled as a slightly flattened spherical vortex at the head of a quasi-steady plume (see figure 1*b*). In Turner's original model, it was assumed that the trailing plume feeds mass, momentum and circulation into the spherical head vortex, and that the velocity of the head vortex, u_b at the base of the vortex is a constant fraction, A_b, of the mean velocity of the trailing plume at the base of the vortex, W_{cb}, i.e.

$$A_b = u_b / W_{cb} = \text{constant}. \tag{14a}$$

With this conceptualization, the velocities at the center and front of the head vortex, u_c and u_t, respectively, will also be proportional to the plume velocity, W_{cc} and W_{ct}, at the equivalent height. Using A_c and A_t to denote the ratios correspondingly, we have

$$A_c = u_c / W_{cc}, \tag{14b}$$

$$A_t = u_t / W_{ct}. \tag{14c}$$

These ratios, A_b, A_c and A_t were all assumed constant throughout the evolution of the starting plume.

For a starting forced plume, the constant assumption for the ratios is invalid because the forced plume has different phases of development, as shown in figure 1(*b*), and the ratios will vary because of the change in the characteristics of the head vortex from puff to thermal and the trailing forced plume from jet-like to plume-like. We shall now relax the assumption that the velocity ratios are constant and compute them directly from the conservation equations.

The variations in A_b, A_c and A_t can be determined by considering the centreline velocity decay, equations (8*a*), (11), (13) and the growth rate of the cap radius. Taking $\alpha' = \mathrm{d}r_v/\mathrm{d}Z$ as the spreading rate of the visible cap edge, we have

$$u_b = u_c \frac{Z_b}{Z_c} = u_c \frac{Z_c - r_v}{Z_c} = u_c \frac{Z_c - Z_c\alpha'}{Z_c} = u_c(1-\alpha'), \tag{15a}$$

and

$$u_t = u_c \frac{Z_t}{Z_c} = u_c \frac{Z_c + r_v}{Z_c} = u_c \frac{Z_c + Z_c\alpha'}{Z_c} = u_c(1+\alpha'). \tag{15b}$$

From (8*a*),

$$\left.\begin{aligned} W_{cb} &= W_{cc}/(1-\alpha')10^{-g(\xi_b)+g(\xi_c)},\\ W_{ct} &= W_{cc}/(1+\alpha')10^{-g(\xi_t)+g(\xi_c)}, \end{aligned}\right\} \quad \text{(for trailing forced plumes)} \tag{16}$$

where $\xi_c = \log(Z_c/L_m)$ and $\xi_b = \log(Z_b/L_m)$. Substituting the above equations into (15*a*) and (15*b*), the relationships for the ratios can be converted to

$$A_b = A_c(1-\alpha')^2 10^{-g(\xi_c)+g(\xi_b)}, \tag{17a}$$

$$A_t = A_c(1+\alpha')^2 10^{-g(\xi_c)+g(\xi_t)}. \tag{17b}$$

By the same reasoning, from (11) and (13) we have

$$W_{cb} = W_{cc}/(1-\alpha'), \quad W_{ct} = W_{cc}/(1+\alpha') \text{ for pure jets} \tag{18a}$$

$$W_{cb} = W_{cc}/(1-\alpha')^{1/3}, \quad W_{ct} = W_{cc}/(1+\alpha')^{1/3} \text{ for pure plumes.} \tag{18b}$$

Equations (17*a*) and (17*b*) can be simplified by combining the above equations for a pure jet or pure plume

$$A_b = A_c(1-\alpha')^2, \quad A_t = A_c(1+\alpha')^2 \text{ for trailing pure jets,} \tag{19a}$$

$$A_b = A_c(1-\alpha')^{4/3}, \quad A_t = A_c(1+\alpha')^{4/3} \text{ for trailing pure plumes.} \tag{19b}$$

Both the momentum and buoyancy fluxes of the leading vortex would be increased owing to the feeding by the trailing forced plume. The buoyancy flux through the base of the head vortex can be computed as (see figure 1*b*(iii))

$$B_v = B_0\frac{(W_{cb}-u_b)}{W_{cb}} = B_0(1-A_b), \tag{20}$$

where t_v represents the time which the head vortex has taken to reach the location from its source.

The velocity of the trailing forced plume stem at the base of the head vortex is faster than the vortex by a factor of A_b at any particular time. The rise time for the trailing forced plume, to reach the base of the head vortex t_j can be related to t_v as

$$t_j = A_b t_v. \tag{21}$$

All the trailing forced plume quantities evaluated at the base of the head vortex may therefore be written as a function of t_v.

The vortex length scale R bears a constant relationship to the Gaussian velocity width of the trailing forced plume (Turner 1962). This relationship can be expressed as

$$R = C_2 b_w. \tag{22}$$

For a pure plume, Turner (1962) suggested that $C_2 = 1.2$.

The rate of change of the head vortex momentum flux can be expressed as:

$$\mathrm{d}M_v/\mathrm{d}t_v = \rho_\infty F_v + \rho\tfrac{1}{2}\pi b_w^2 W_{cb}^2(1-A_b), \tag{23}$$

where ρ can be considered as the average density at the base of the head vortex. The first and second terms of the right-hand side of (23) represent the action of the buoyant force and the rate of injection of momentum flux from the trailing forced plume, respectively.

The buoyancy force of the head vortex can be calculated by integrating (20), to give,

$$F_v = \int_0^{t_v} B_0(1-A_b)\,\mathrm{d}t_v'. \tag{24}$$

Using the behaviour of steady forced plumes (equation (8*a*)) and replacing b_w with $\eta_{wg}Z$, equation (23) can be integrated to become

$$M_v = \rho_\infty B_0\int_0^{t_v}\left(\int_0^{t_v}(1-A_b)\,\mathrm{d}t_v'\right)\mathrm{d}t_v'' + \tfrac{1}{2}\pi\rho\eta_{wg}^2 M_0^{1/2}\int_0^{Z_b}(1-A_b)/A_b 10^{-g(\xi_b)}Z_b'\,\mathrm{d}Z_b'. \tag{25}$$

Incorporating (6) into (25) yields,

$$(\pi\rho_v/C_1)R^3u_c = \rho_\infty B_0\int_0^{t_v}\left(\int_0^{t_v}(1-A_b)\,\mathrm{d}t_v'\right)\mathrm{d}t_v'' + \tfrac{1}{2}\pi\rho\eta_{wg}^2 M_0^{1/2}\int_0^{Z_b}(1-A_b)/A_b 10^{-g(\xi_b)}Z_b'\,\mathrm{d}Z_b'. \tag{26}$$

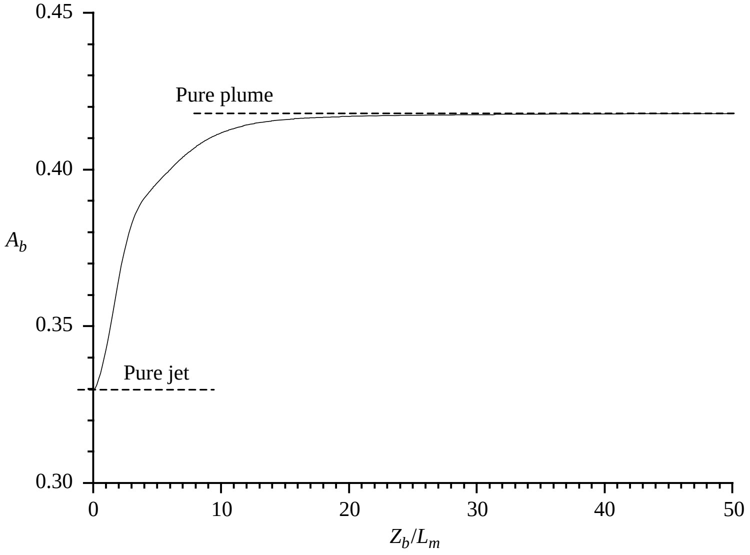

FIGURE 2. Variation of A_b with Z_b/L_m.

Thus, the relationship between Z_b and t_v can be computed as:

$$t_v = \int_0^{Z_b} \frac{1}{u_b}\,\mathrm{d}Z_b' = \int_0^{Z_b} \frac{\mathrm{d}Z_b'}{A_b W_{cb}}. \tag{27}$$

Replacing t_v, R and u_c with Z_b, b_w and W_{cb}, respectively, (26) can be transformed to,

$$\left(\frac{\pi\rho_v}{C_1}\right) C_2^3 \eta_{wg}^3 \frac{A_b}{1-\alpha'} 10^{-g(\xi_b)} \bar{Z}_b^2 = \rho_\infty B_0 \int_0^{\bar{Z}_b} \left(\int_0^{\bar{Z}_b} (1-A_b) \frac{Z_b'\,\mathrm{d}Z_b'}{A_b 10^{-g(\xi_b)}} \right) \frac{Z_b''\,\mathrm{d}Z_b''}{A_b 10^{-g(\xi_b)}} + \tfrac{1}{2}\pi\rho\eta_{wg}^2 M_0^{1/2} \int_0^{\bar{Z}_b} (1-A_b)/A_b 10^{-g(\xi_b)} Z_b'\,\mathrm{d}Z_b', \tag{28}$$

where $\bar{Z}_b = Z_b/L_m$.

For Boussinesq starting forced plumes, $\rho_v \approx \rho_\infty \approx \rho$, equation (28) can then be written as

$$\left(\frac{\pi}{C_1}\right) C_2^3 \eta_{wg}^3 \frac{A_b}{1-\alpha'} 10^{-g(\xi_b)} \bar{Z}_b^2 = B_0 \int_0^{\bar{Z}_b} \left(\int_0^{\bar{Z}_b} (1-A_b) \frac{Z_b'\,\mathrm{d}Z_b'}{A_b 10^{-g(\xi_b)}} \right) \frac{Z_b''\,\mathrm{d}Z_b''}{A_b 10^{-g(\xi_b)}} + \tfrac{1}{2}\pi\eta_{wg}^2 M_0^{1/2} \int_0^{\bar{Z}_b} (1-A_b)/A_b 10^{-g(\xi_b)} Z_b'\,\mathrm{d}Z_b'. \tag{29}$$

Taking the values of $C_1 = 0.14$, $C_2 = 1.2$ from Turner (1962), $\eta_{wg} = 0.105$ from Wang & Law (2002), and $\alpha' = 0.16$ from the present experiments (further discussion will be provided in § 6.1.2), the value of A_b can be computed from (29) using iteration methods.

Figure 2 shows the results of the iterations. It can be seen that the value of A_b starts at 0.33 in the jet-like region, increases throughout the transition and then reaches a steady value of 0.418 in the plume-like region when $Z_b/L_m > 30$. In other words, the head vortex is being injected with a progressively larger amount of mass and momentum fluxes by the trailing stem as the forced plume enters into the jet-like, transitional and plume-like phases consecutively. It is important to note that Turner

(1962) obtained a measured value of 0.38 for A_b which is approximately in the middle of the computed range (0.33–0.418). The value of 0.418 is in excellent agreement with the maximum theoretical value (0.42) derived by Delichatsios (1979) in his analytical work on starting plumes. His theoretical value was obtained by applying a shock (jump) condition at the base of the vortex with the value of buoyancy after the shock assumed to be 0. In reality, the shock would not be so abrupt and thus the value of A_b can only approach 0.42 asymptotically.

Let us verify the computational results in figure 2 in the asymptotic phases (i.e. jet-like and plume-like regions). The rate of change of momentum flux for the head vortex as a momentum puff, i.e. $B_v = 0$, (equation (23)) can be simplified to

$$\mathrm{d}M_v/\mathrm{d}t_v = \tfrac{1}{2}\pi\rho b_w^2 W_{cb}^2 (1 - A_b). \tag{30}$$

Substituting (11) into (30), we obtain

$$\int_0^{\bar{\bar{\bar{Z}}}_b} \frac{1 - A_b}{2A_b} Z_b' \mathrm{d}Z_b' = \frac{C_2^3}{C_1} \frac{A_b}{1 - \alpha'} \eta_{wg} (\bar{\bar{\bar{Z}}}_b)^2, \tag{31}$$

where $\bar{\bar{\bar{Z}}}_b = Z_b/D$. From (31), A_b can be solved analytically as,

$$A_b = \frac{-1 + \sqrt{\dfrac{16\eta_{wg}C_2^3}{C_1(1-\alpha')} + 1}}{\dfrac{8\eta_{wg}C_2^3}{C_1(1-\alpha')}} = 0.33. \tag{32}$$

The value of 0.33 is identical to the value determined by the iteration methods shown in figure 2. With the same reasoning, replacing $g(\xi)$ in (29) with the results of a steady pure plume (equation (12)), A_b can be obtained as a constant with the magnitude of 0.418.

Given the value of A_b, the velocity at the base of the head vortex can be determined:

$$u_b = A_b W_{cb} = A_b 10^{-g(\xi_b)} Z^{-1} M_0^{1/2}. \tag{33}$$

Substituting the results of the forced plume velocity (equation (33)) into (27), the penetration rate for a starting Boussinesq forced plume can finally be obtained as,

$$\bar{t}_v = \int_0^{\bar{Z}_b} \frac{Z_b' \mathrm{d}Z_b'}{A_b 10^{-g(\xi_b)}} = \int_0^{\bar{Z}_t} \frac{Z_t'(1-\alpha')/(1+\alpha')\mathrm{d}[Z_t'(1-\alpha')/(1+\alpha')]}{A_b 10^{-g(\xi_b)}}, \tag{34}$$

where $\bar{t}_v = t_v B_0/M_0$ and $\bar{Z}_t = Z_t/L_m$ are normalized travelling time and distance for the front of the head vortex, respectively.

The penetration behaviour described by (34) is plotted in figure 3. The penetration time derived in (34) covers the various phases in PDF. For verification, we shall now compare the predictions of the penetration time to the measurements of starting jets and starting plumes reported in the literature.

Incorporating the asymptotic jet-like behaviour, i.e. (10), equation (34) becomes,

$$\bar{\bar{t}}_v = \int_0^{\bar{\bar{\bar{Z}}}_b} \frac{Z_b' \mathrm{d}Z_b'}{A_b k_{jw}} = \frac{1}{2A_b k_{jw}} [\bar{\bar{\bar{Z}}}_t (1-\alpha')/(1+\alpha')]^2, \tag{35}$$

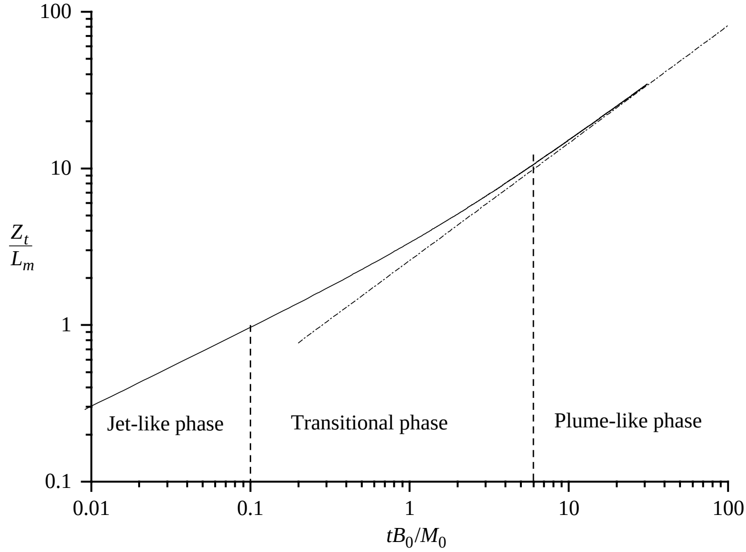

FIGURE 3. Penetration rate of a fully-developed starting plume. —, equation (34); –·–, equation (38).

where $\bar{\bar{t}}_v = t_v W_0/D$ and $\bar{\bar{Z}}_t = Z_t/D$. Using 0.33, 6.477 and 0.16 to replace the constants A_b, k_{jw} and α', respectively, (35) gives

$$\bar{\bar{Z}}_t = 2.853(\bar{\bar{t}}_v)^{1/2}. \tag{36}$$

For the numerical coefficient in (36), Sangras *et al.* (2003) obtained a value of 2.6 from their experiments on starting jets, which is approximately 10 % less that the prediction in (36), while Lahbabi, Boree & Charnay (1993) measured a value of 2.9 and Witze (1980) from 2.5 to 3.2, which are nearly identical to the present analytical results. Note that Sangras *et al.* used a video-based technique for their laboratory measurements and thus it can be expected that the accuracy was lower than for the other more advanced imaging techniques such as PLIF.

For plume-like behaviour, incorporating (12), equation (34) simplifies to,

$$\bar{t}_v = \int_0^{\bar{Z}_b} \frac{(Z_b')^{1/3}\,\mathrm{d}Z_b'}{A_b k_{pw}} = \frac{3}{4}\frac{1}{A_b k_{pw}}[\bar{Z}_t(1-\alpha')/(1+\alpha')]^{4/3}. \tag{37}$$

Substituting the constants ($A_b = 0.418$, $k_{pw} = 4.13$ and $\alpha' = 0.16$) into (37), yields,

$$\bar{Z}_t = 2.579(\bar{t}_v)^{3/4}. \tag{38}$$

The numerical coefficient in (38) is very close to Middleton's (1975) results on starting pure plumes. From analytical derivations, Middleton concluded that the velocity of the head vortex for a starting plume decays in the following manner

$$u_c = \frac{5^{1/2}}{2\alpha^{1/2}\pi^{1/4}} A_c B_0 (t_v)^{-1/4}. \tag{39}$$

Based on Turner's experimental results, $\alpha = 0.09$ and $A_c = 0.49$, equation (39) can be converted to,

$$\overline{Z}_t = 2.536(\bar{t}_v)^{3/4}. \tag{40}$$

It can be seen that. (38) and (40) are nearly identical.

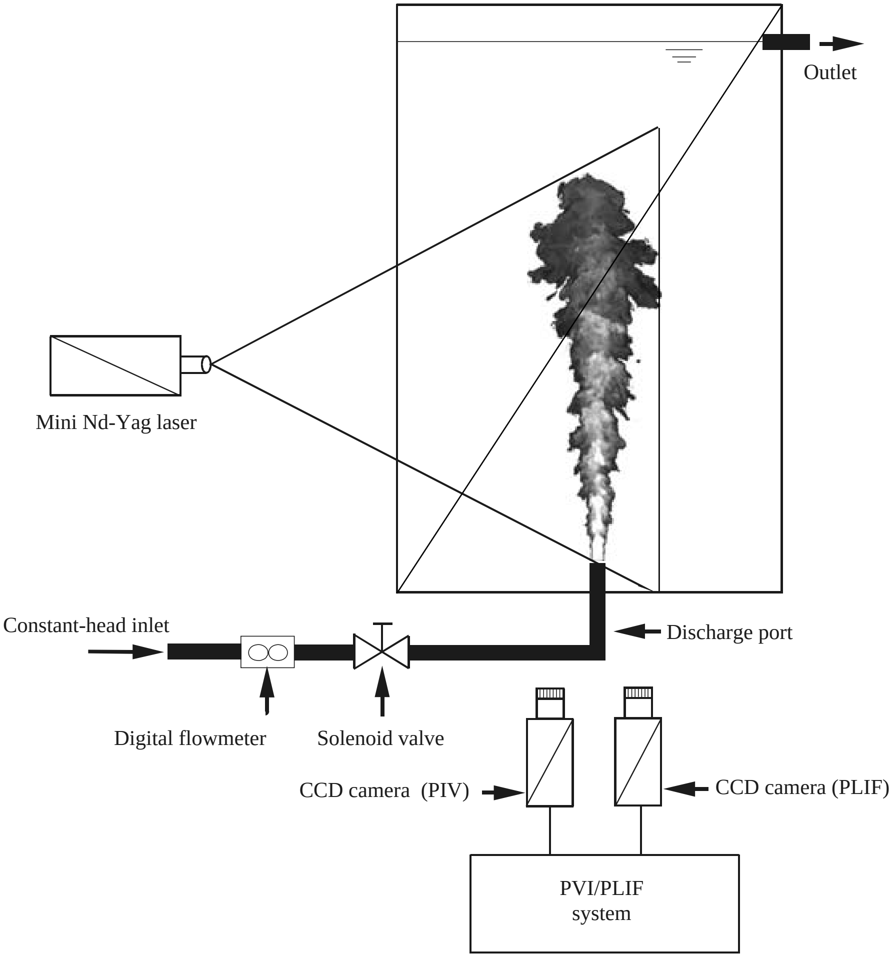

FIGURE 4. Experimental set-up.

The unified penetration time given in (34) covers the three different phases in PDF including jet-like, transitional and plume-like. Although laboratory measurements on starting jets and starting plumes have been reported previously, no information on the transitional phase can be found in the literature as far as we are aware. In the following, we shall report an experimental investigation with PIV and PLIF that will provide information on the full range of development of a starting forced plume.

5. Experiments on starting forced plumes

A schematic diagram of the experimental set-up is shown in figure 4. The experiments were conducted in a glass test tank with dimensions of $0.55\,\mathrm{m} \times 0.55\,\mathrm{m} \times 1.2\,\mathrm{m}$ (height). The tank was constructed of glass panels with a stainless steel frame. The source solution was discharged from a round nozzle seated at the bottom of the tank. The nozzle was 100 mm in length and had a diameter of 7.5 mm. The source fluid was supplied from a constant head tank located 2.8 m above the test tank. The water temperature was kept constant at about 25 °C to avoid the influence of temperature on dye fluorescence. The volumetric flow rate was controlled by a needle valve and monitored by a digital flow meter (model Endress + Hauser Promag 33). A solenoid valve with an opening time of about 20 ms was used to ensure that the starting process could be considered to be near instantaneous.

The velocity and concentration measurements were based on a combined PIV/PLIF approach (Law & Wang 2000). The light source employed a dual-cavity pulsed mini Nd:YAG laser with a maximum repetition rate of 15 Hz for each cavity. The energy level was 50 mJ per pulse and the pulse duration was about 7 ns. The emitted laser light was green with a wavelength of 532 nm. The light sheet had a typical thickness of 3 mm and a divergence angle of 32°.

Two double-frame 8-bit digital CCD cameras (Kodak Megaplus ES1.0) were configured, one for PIV and the other for PLIF. The spatial resolution of the cameras was 1008×1016 pixels. Both cameras were fitted with a Nikon 60 mm lens. The PLIF camera was set to single-frame mode while the PIV camera worked in double-frame mode. Thus, the PLIF image was double-exposed by the laser pulse pair, the interval of which was determined by the cross-correlation PIV requirement. The two cameras were pointed to nearly the same area with a typical size of $30\,\text{cm} \times 30\,\text{cm}$.

Adaptive cross-correlation was employed to analyse the PIV images. Using a window size of 32×32 pixels and a step size for the moving average of 16×16 pixels (50 % window overlap), the processing resulted in a field measurement of 62×62 velocity vectors with a temporal resolution of 5.0 Hz. The time interval between two successive exposures was set properly in order to limit the maximum displacement of particles within a quarter of the window size (i.e. 8 pixels, as shown in table 1).

Polyamid seeding particles (PSP, with average diameter of 50 μm) and Rhodamine B were selected as the tracers for PIV and PLIF. The absorption spectrum of Rhodamine B is from 460 to 590 nm with a peak at 550 nm, while its emission spectrum ranges from 550 nm to 680 nm with a peak at 590 nm. An optical 532 nm band-pass filter was placed in front of the PIV camera, allowing only a narrow band of wavelengths around 532 nm scattered by the seeding particles to pass through. Another optical 590 nm high-pass filter was attached to the PLIF camera, allowing through only the fluorescent light emitted from the dye tracer.

A total of 11 tests were performed and the experimental parameters are given in table 1. The first seven cases had a relatively small density difference of up to 15 %. In these cases, saline was employed as the ambient solution and fresh water as the plume fluid. This combination of fresh and saline water is commonly adopted for experimentation on forced plumes within the Boussinesq range (e.g. Wang & Law 2002; Diez *et al.* 2003).

We also conducted four experiments with larger density differences (20 % and 25 %) to investigate the behaviour of non-Boussinesq starting forced plumes. In order to include these higher density difference cases, a combination of light-weight ethanol solution and heavy calcium chloride solution was used instead. The two solutions were chosen because they can have a similar refractive index while having vastly different densities depending on the concentrations of ethanol and calcium chloride, as shown in figure 5. The matching refraction index was required in order to avoid optical distortion of the PIV/PLIF images.

6. Experimental results and discussions

The general observation of a typical starting forced plume in the experiments is shown in figure 6 (Case C3). The first image (figure 6-001) was recorded at 0.2 s after the forced plume was initiated. The series of images had a time interval of 0.2 s. In

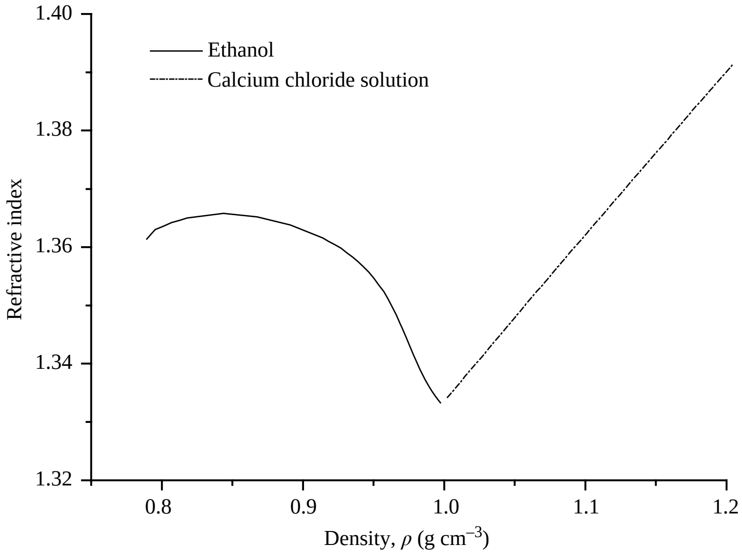

FIGURE 5. Refractive indices versus densities of –·–, calcium chloride and —, ethanol.

the beginning, the forced plume was pushed upward into the ambient fluid by the initial momentum flux, and a puff was formed with the intrusion. The starting forced plume then began to initiate a complex sequence of vortex leapfrog, coalescence, pinch-off and reconnection (cf. figure 1*a* and Ai *et al.* 2005). During this developing period, the penetration accelerated to a maximum value and then started to decelerate towards the temporal behaviour of the developed flow. This phenomenon of initial acceleration is called overshooting. In addition to the penetration rate, overshoot is also commonly observed in the growth of the head vortex size (Maxworthy 1977; Didden 1979; Ai *et al.* 2005). In our experiments, overshoot was typically recorded in the penetration results (cf. § 6.1.1).

From the images, a trailing jet was formed behind the head intrusion (see figure 6) immediately after the forced plume was started. After some time, a cap vortex became distinguishable with an obvious boundary (as indicated by the circle in figure 6-009). At the same time, the advancing head vortex was fed with fluid from the trailing forced plume which added buoyancy and momentum fluxes to the vortex. The flow-visualization records showed that the cap vortex grew continuously in size, and then emanated into the ambient fluid at the time of the pinch-off (see figure 6-003). The detachment occurred momentarily and visibly (although in some cases the pinch-off could not be observed well because of the instant reconnection) and the head vortex was subsequently reconnected (see figure 6-004) to the stem which completed the developing phase in PFD. After the reconnection, a new head vortex was formed engulfing the initial vortex while leading the trailing forced plume.

We shall now address the Boussinesq and non-Boussinesq cases separately in the following with demarcation for the two cases set at 15 %. The judgment is based on the experimental observations of the behaviours of the starting forced plume or the trailing buoyant jet, i.e. the penetration rate and centreline velocity. As presented in the following, we observed distinct differences between plumes having an initial density of larger or smaller than 15 %, and thus the value was adopted as an approximate criterion whether the Boussinesq approximation for small density differences can be made or not.

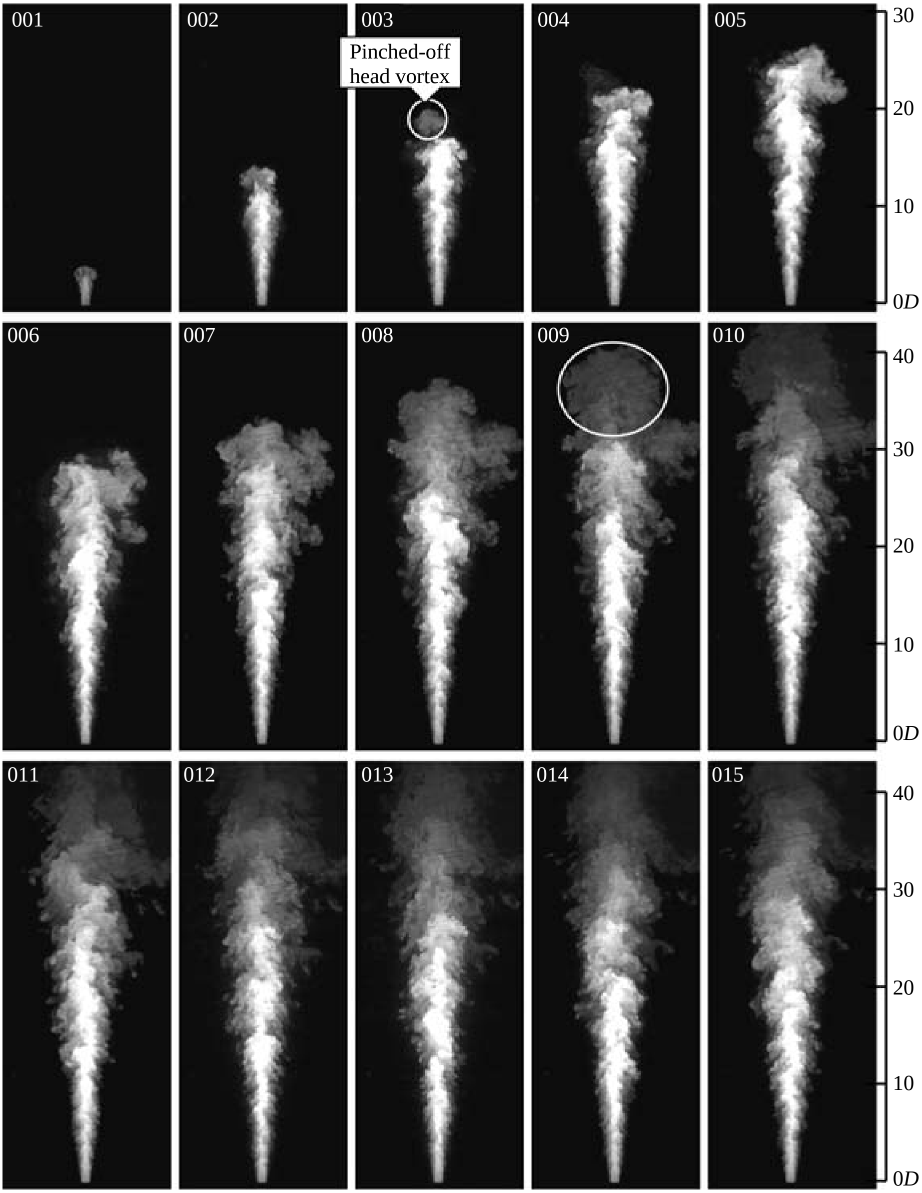

FIGURE 6. Sequence of PLIF images through the central axis of symmetry showing the evolution of a starting plume for Case C3. The first image was 0.2 s after the initial start of the plume. The time interval of the images is 0.2 s.

6.1. *Boussinesq starting forced plumes*

6.1.1. *Streamwise penetration of head vortex*

For Boussinesq starting forced plumes, Diez *et al.* (2003) proposed the penetration time as:

$$(Z_t - Z_0)/D = C_z(t/t^*)^{3/4}, \tag{41}$$

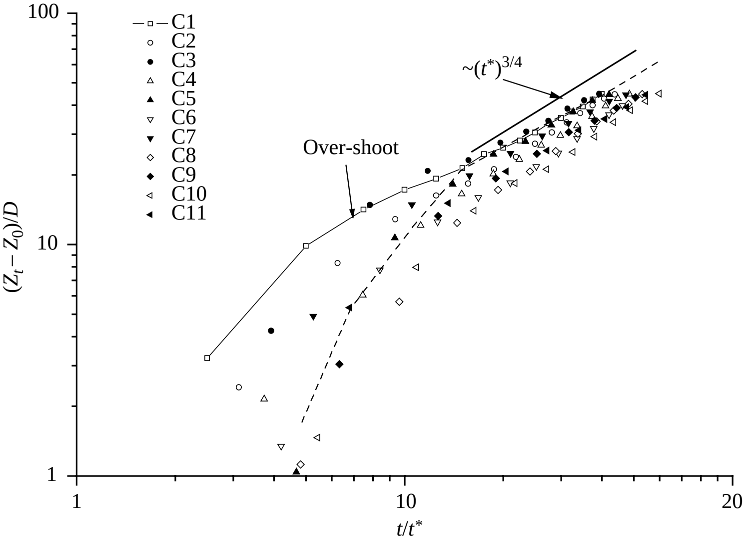

FIGURE 7. Normalized streamwise penetration distance $(Z_t - Z_0)/D$ as a function of normalized time t/t^*. - - -, Diez *et al.* (2003).

where C_z and Z_0 are best-fit empirical parameters of self-preserving scaling relationships, t^* is defined as:

$$t^* = (D^4/B_0)^{1/3}. \tag{42}$$

Using this time scale, the experimental results on the penetration rate are plotted in figure 7. The virtual origin was set as $Z_0/D = 7.0$ in this figure following the suggestion by Diez *et al.* (2003). It can be seen that although the time exponent can be fitted to be 3/4, the coefficient C_z does not appear to be a constant. Note that the knee at $t/t^* \approx 10$ signifies the developing period of the forced plume. This knee can be related to the overshoot phenomenon as mentioned above. In all experiments, the developing phase of the forced plume dominated the initial period such that the jet-like phase was not observed and the characteristics in this phase need to be further explored in the future.

Using L_m as the length scale, figure 8 shows the penetration height as a function of time for the Boussinesq cases. A time scale, defined as M_0/B_0 (Pantzlaff & Lueptow 1999), can be used to identify the three developed phases of the forced plume (Fischer *et al.* 1979). The jet-like phase occurs when $t \ll M_0/B_0$, while the transitional phase is dominated by both initial momentum and buoyancy fluxes when $t \sim M_0/B_0$. When $t \gg M_0/B_0$, the forced plume becomes similar to a starting pure plume.

It can be observed that the analytical model in (34) gives a reliable prediction on the behaviour of the starting forced plume in PDF, including the transitional phase as well as the asymptotic plume phase. Note that the virtual origin correction, which is commonly adopted by the previous models in the literature, is not required here owing to the detailed simulation of the different phases. As shown in figure 8, the experimental data in the present experiments (cases with $\Delta_0 \leqslant 15\%$) are in excellent agreement with (34) in the PDF, while in the PFD, the starting forced plume behaves differently as expected.

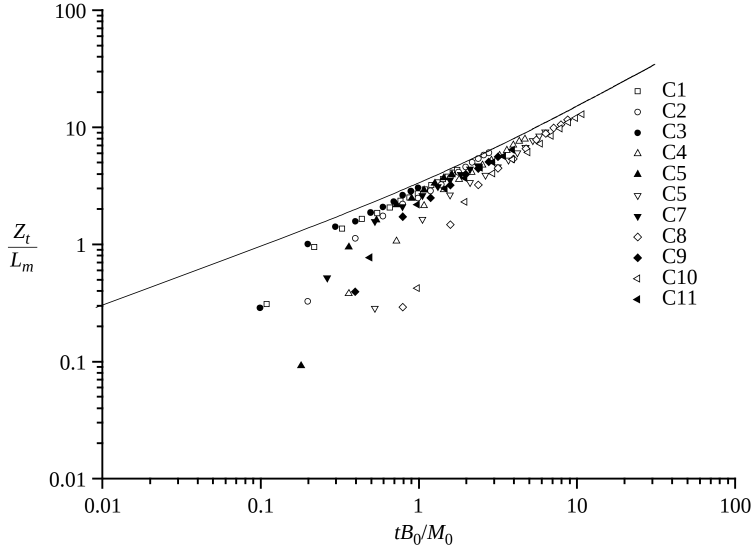

FIGURE 8. Normalized streamwise penetration distance Z_t/L_m as a function of normalized time tB_0/M_0. —, equation (34).

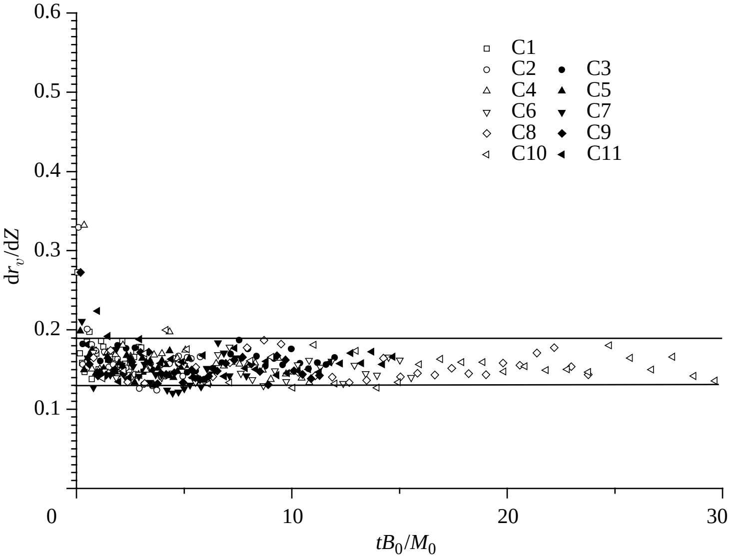

FIGURE 9. Radial penetration *vs.* tB_0/M_0.

6.1.2. *Radial penetration*

The corresponding temporal variation of the maximum radial penetration distance can be expressed in terms of the streamwise penetration distance, as follows:

$$(r_v - D/2)/Z = \frac{dr_v}{dZ} = \alpha', \tag{43}$$

where α' is the spreading rate of the trailing forced plume, and Z is the local height (rather than the distance to the vortex front). For both starting and steady plumes, α' is typically taken to be a constant. Figure 9 shows the values of α' to be approximately

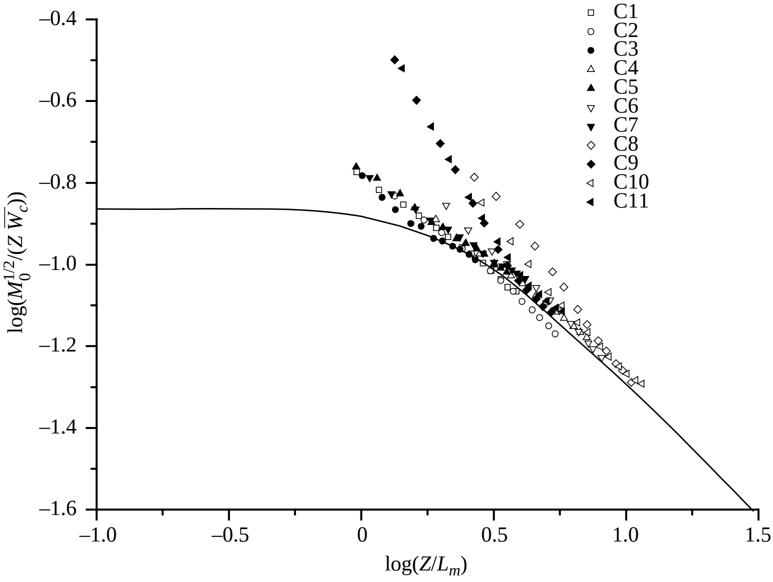

FIGURE 10. Centreline decay of mean axial velocity with equation (8*a*). —, Wang & Law (2002).

0.16 ± 0.03 in PDF, in reasonable agreement with Diez *et al.* (2003) and Turner (1962) who obtained 0.16 and 0.18 for starting plumes, respectively. From figure 9, it can also be seen that due to the initial vortex dynamics, the spreading rate of the head vortex in PFD was larger. Subsequently, as the pinch-off occurred and the feeding of buoyancy and circulation into the head vortex ceased, the spreading rate began to decrease because of the lower entrainment until the head vortex reconnected with the trailing stem. Throughout the development, the Gaussian velocity width also showed a monotonic increase until it reached the steady-state values (cf. § 6.6).

6.1.3. *Boussinesq trailing forced plumes*

For the Boussinesq cases, the mean axial velocity decay along the centreline of the trailing forced plume is plotted in figure 10. In the figure, the solid line represents the results of Wang & Law (2002) for a steady buoyancy jet. They reported that for $Z/L_m < 0.6$ the flow is jet-like, and for $Z/L_m > 6$ the flow is plume-like. Near the forced plume exit, the experimental data deviated from the self-similar solution. As mentioned above, this is because the flow in this zone has not established self-similarity and thus the similarity solutions are not applicable. Similar to the results of the penetration rate for the non-Boussinesq cases, the mean centreline velocity became self-similar at the location of $Z/L_m \approx 2$. Figure 10 shows that the trailing forced plume overshot the jet-like area and entered the transitional phase in PDF directly. The figure further implies that the stronger the initial momentum, the shorter the dimensionless time of the PFD would be.

Figure 11 shows the variation of the axial velocity with the plume penetration. The figure was plotted according to the similarity solution

$$\frac{W_c}{W_0} = k_{pw}\left(\frac{\pi}{4}\right)^{1/3} Fr_0^{-2/3}\left(\frac{Z}{D}\right)^{-1/3}, \tag{44}$$

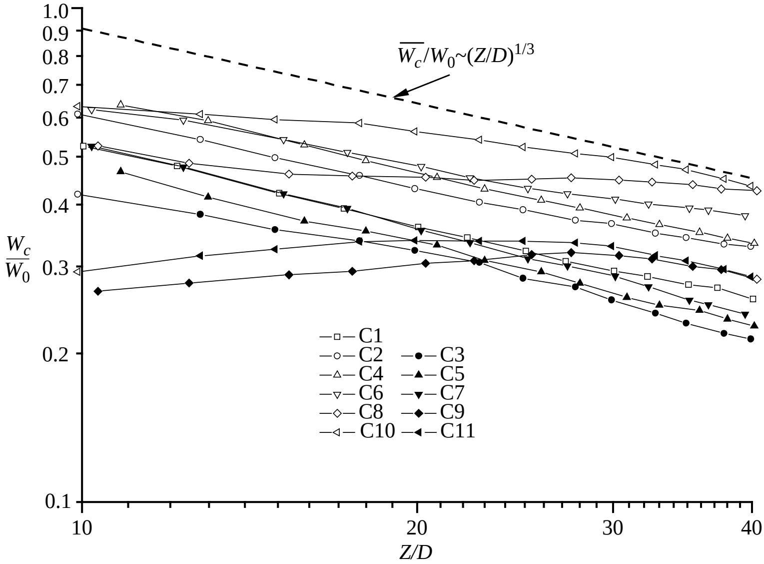

FIGURE 11. Normalized centreline velocity decay as a function of Z/D.

which is another form of (13) and reflects the variation of the actual mean centreline velocity. The Froude number Fr_0 reads

$$Fr_0 = \frac{W_0}{\sqrt{\Delta_0 D}}. \tag{45}$$

The graph illustrates that the non-dimensional centreline velocity developed as expected when $\Delta_0 \leqslant 15\%$ (i.e. Boussinesq cases). The order of the lines depends on initial Froude numbers (as shown in table 1). However, it shows totally different characteristics for the non-Boussinesq cases. The details for the non-Boussinesq cases will be presented in § 6.2.3.

6.2. *Non-Boussinesq starting forced plumes*

6.2.1. *Streamwise penetration of head vortex*

As shown in figure 8, the experimental results for the non-Boussinesq cases showed larger deviation than the Boussinesq cases with similar initial velocity. The differences between the Boussinesq and non-Boussinesq forced plumes occurred mainly in the region near the source and were due to the strong non-Boussinesq effects. The reinforced buoyancy initially accelerated the leading vortex (puff) and boosted the penetration rate. With continuous dilution, the non-Boussinesq effects diminished away from the source. Thus, the difference between the two cases can be corrected by the virtual origin method to account for the near-field effects.

Carlotti & Hunt (2005) replaced the actual non-Boussinesq area source located at $Z = 0$ with an idealized point source located at a virtual origin $Z = Z_0$, and proposed the asymptotic analytical expressions for the pure, lazy and forced plumes valid for large vertical distances above the non-Boussinesq source. A characteristic length scale, related to the buoyancy B_0 and gravity g, is proposed as:

$$\ell_0 = \frac{B_0^{2/5}}{(C_3 g)^{3/5}}, \tag{46}$$

Case	Q_0 (cm^3 s^{-1})	g_0' (cm s^{-2})	B_0 (cm^4 s^{-3})	M_0 (cm^4 s^{-2})	ℓ_0 (mm)	Z_0/L_m
C8	22.22	198.16	4403.5	1117.7	16.9	−1.668
C9	43.61	198.16	8641.6	4304.9	22.0	−1.390
C10	22.22	245.69	5459.7	1117.7	18.3	−1.662
C11	43.61	245.69	10714.4	4304.9	24.0	−1.384

TABLE 2. Virtual origin correction for starting plumes.

where the constant $C_3 = 0.1154$, was employed to normalize the mass and momentum fluxes, i.e.

$$\wp_0 = \frac{g\dfrac{\rho_0}{\rho_\infty}Q_0}{(C_3 g)^{3/2}\ell_0^{5/2}} \text{ (dimensionless mass flux),} \tag{47a}$$

$$\lambda\!\!\!^{-}_0 = \frac{M_0}{C_3^{3/2} g \ell_0^{5/2}} \text{ (dimensionless momentum flux).} \tag{47b}$$

According to Carlotti & Hunt (2005), the virtual origin for the non-Boussinesq steady forced plumes can be expressed as,

$$\frac{Z_0}{\ell_0} = -\tfrac{3}{5}\left(\lambda\!\!\!^{-}_0{}^{5/2} - \wp_0^2\right)^{3/10} \int_0^{\wp_0/(\lambda\!\!\!^{-}_0{}^{5/2} - \wp_0^2)^{1/2}} \frac{\mathrm{d}x}{(x^2+1)^{1/5}} + \tfrac{3}{5} C_4 \left(\lambda\!\!\!^{-}_0{}^{5/2} - \wp_0^2\right)^{3/10}, \tag{48}$$

where the constant $C_4 = -0.84$. Table 2 gives the values of Z_0/L_m. Further discussion for the virtual origin correction of the non-Boussinesq steady plume was also presented in Carlotti & Hunt (2005).

The above virtual origin determination was developed for a non-Boussinesq steady forced plume. For non-Boussinesq ‘starting’ forced plumes, it is uncertain whether a similar approach can be adopted or not. Using the correction results of Z_0/L_m in table 2, the non-Boussinesq effects on the starting forced plume penetration rates are illustrated in figure 12(*b*). For the convenience of comparison, the original data for the non-Boussinesq cases were extracted from figure 8 and plotted in figure 12(*a*). When comparing figure 12(*b*) with figure 12(*a*), the corrected penetration rates fitted significantly better with the model prediction for Boussinesq plumes (equation (34)). Hence, the experimental results show that the virtual origin correction can also be applied for the penetration rate of non-Boussinesq starting forced plumes.

6.2.2. *Radial penetration*

Figure 9 shows that the radial penetration in terms of the spreading rate is the same ($\alpha' = 0.16 \pm 0.03$) for both Boussinesq and non-Boussinesq starting forced plumes in PDF. It is, however, important to note that flapping, a phenomenon which is related to the large-scale vortices and can significantly increase the spreading rate in steady plumes (Papps & Wood 1997), was also commonly observed in our experiments on starting forced plumes. In PFD where the non-Boussinesq effects were more significant owing to the higher density differences, we noted an important observation that significantly more flapping was observed in non-Boussinesq cases than in Boussinesq cases (shown in figures 13*a* and 13*b*). However, although the magnitude of the flapping motion was stronger in non-Boussinesq cases, the spreading rate in PDF did not increase according to figure 9. This may be because the strong buoyancy in the

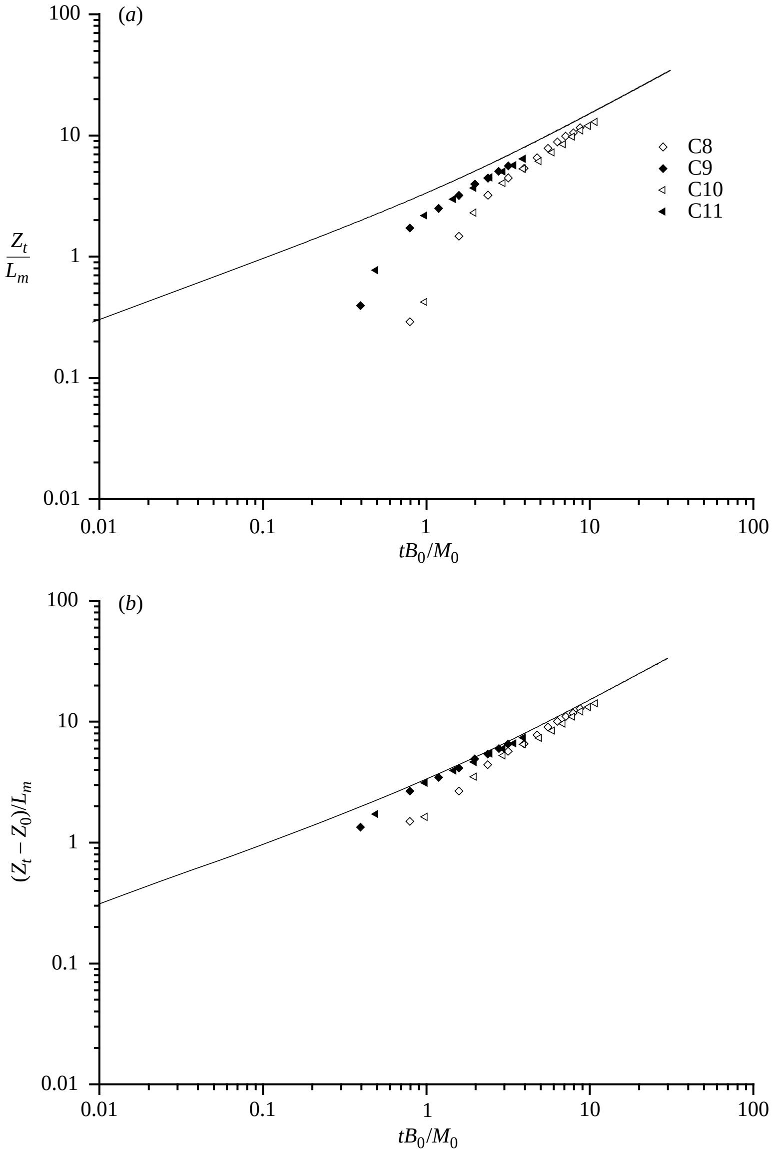

FIGURE 12. Normalized streamwise penetration distance Z_t/L_m as a function of normalized time tB_0/M_0 for non-Boussinesq cases: (*a*) without virtual origin correction (*b*) with virtual origin correction. —, equation (34).

near field pushed the starting forced plume to move up faster, and thus counteracted the increased spreading rate by the flapping motion.

6.2.3. *Non-Boussinesq trailing forced plumes*

The variation of centreline velocity decay with penetration distance for the non-Boussinesq cases is also shown in figure 10. Larger deviations were revealed in the zone of flow establishment where the characteristics of the flow were significantly influenced by the source conditions, i.e. initial momentum, buoyancy, volume fluxes and nozzle geometry, and the flow behaviours were non-self-similar. However, when

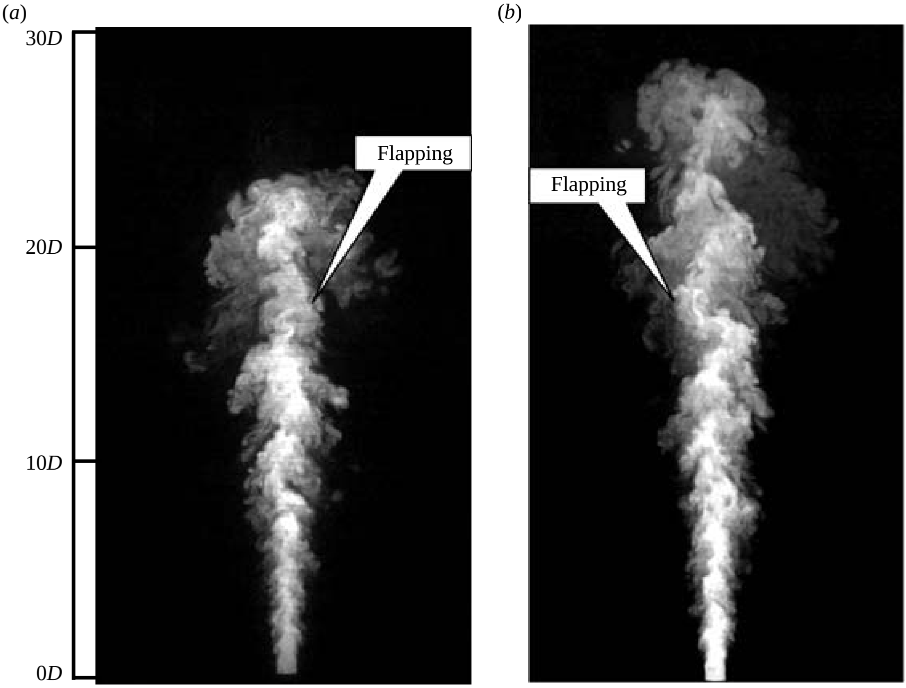

FIGURE 13. Flapping motion in starting plumes: (*a*) $t = 1.4\,\text{s}$ in Case C2 and (*b*) $t = 1.0\,\text{s}$ in Case C9.

the flow entered the zone of established flow, the behaviours became more predictable and the deviations were much reduced. From $Z/L_m > 6$ onward, the data began to follow the asymptotic behaviour of Boussinesq pure plumes with a net displacement due to the virtual origin. As discussed previously, the asymptotic behaviour was due to the continuous dilution with the entrainment of ambient fluid and the diminishing of density differences between the forced plume and the surrounding. In the region near the source, however, the non-Boussinesq effects were prevalent and the strong buoyancy played a significant role in the evolution as evidenced by the deviations in the initial region in figure 10. In the following, we shall examine more closely the non-Boussinesq effect in this region.

As shown in figure 11, it is surprising to note that the behaviour of the centreline velocity for the non-Boussinesq cases dramatically deviated from that of the Boussinesq cases. Instead of decaying in the observational region, the velocity increased or remained steady initially before it began to attenuate. In the initial region of non-Boussinesq starting forced plume, the strong buoyancy overwhelmed the shear stress at the plume edge and led to an increase in the centreline velocity in the beginning (as compared to a decrease for Boussinesq plumes). The velocity eventually reached a peak at $Z/D \approx 30$ in Cases C9 and C11. With the entrainment and the corresponding dilution, the buoyancy began to weaken and then the velocity started to decrease with distance. For Case C8, the centreline velocity remained steady for some time suggesting that the buoyancy force balanced the turbulence shear force during this period. For Case C10, the centreline velocity had a similar trend to that of C8, but decreased at a slower pace. Figures 10 and 11 demonstrated that it would take a longer distance for a strongly buoyant forced plume to develop into the asymptotic states.

Case	Δ_0 (%)	b_w/Z
C1	2.77	0.103
C2	5.48	0.100
C3	5.48	0.101
C4	9.38	0.099
C5	9.38	0.098
C6	13.40	0.102
C7	13.40	0.098
C8	19.45	0.104
C9	19.45	0.100
C10	25.07	0.105
C11	25.07	0.104
Wang & Law (2002)	<3 %	0.105
Fischer *et al.* (1979)	–	0.100

TABLE 3. Comparison of plume width.

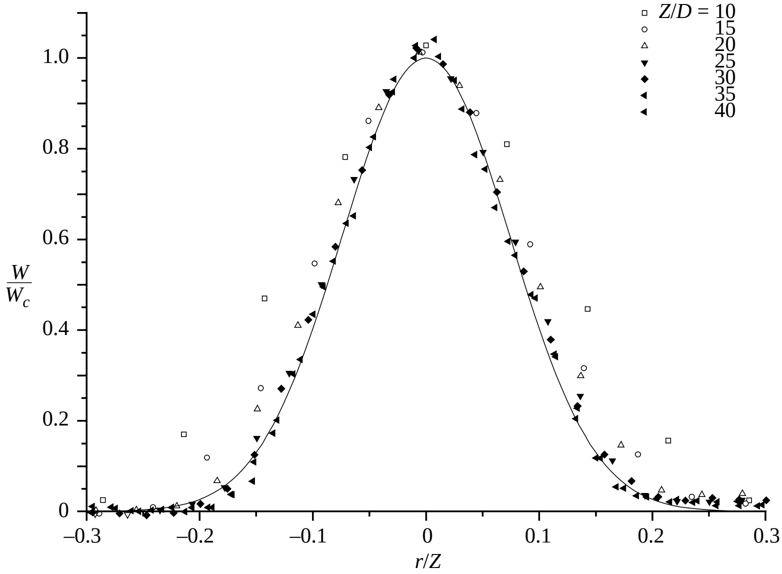

FIGURE 14. Cross-sectional variation of the mean axial velocity in Case C1, showing that the profiles become self-similar when $Z/D > 25$. —, Gaussian fit.

6.2.4. *Plume width and entrainment in non-Boussinesq cases*

Table 3 shows the plume characteristics for the present experiments in PDF. From the table, it can be observed that the velocity radius spreading rate, b_w/Z (fitted by the Gaussian profile as shown in the Appendix), varied from 0.098 to 0.105, and was near Fischer *et al.*'s (1979) suggested range, but slightly smaller than the value of 0.105 obtained by Wang & Law (2002) for steady Boussinesq plumes. The results imply that the proportional constant for the Gaussian radius b_w is nearly the same throughout the three different phases of jet-like, transitional and plume-like.

Figures 14 and 15 demonstrate the Gaussian cross-sectional velocity profiles at different locations for Cases C1 and C11. The expansion in radius was similar for both Boussinesq and non-Boussinesq cases, although the locations where the plumes

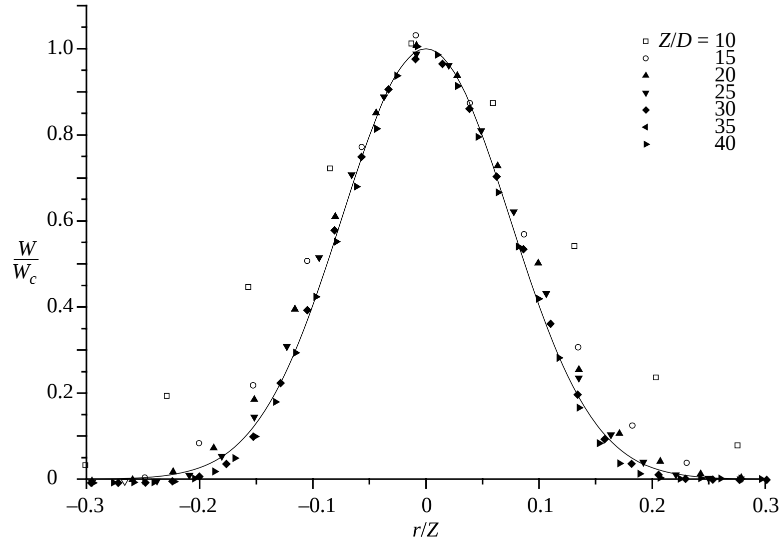

FIGURE 15. Cross-sectional variation of mean axial velocity in Case C11. The profiles became self-similar only after $Z/D > 15$. —, Gaussian fit.

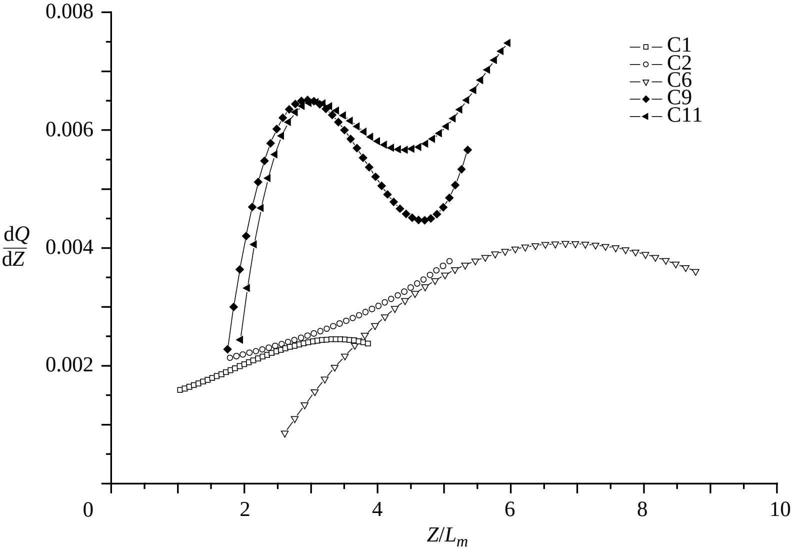

FIGURE 16. Variation of volume entrainment rate with Z/L_m.

became asymptotic were different. The stronger the initial buoyancy, the shorter the distance before the plume developed into a self-preserving state.

Figures 16 and 17 plot the variations of volume entrainment rate and entrainment coefficient (calculated according to (A3)) along the penetration distance, respectively. For Boussinesq cases ($\Delta_0 < 15\,\%$), behaviour was asymptotic (see figures 16 and 17) and nearly identical to previous observations in steady buoyant plumes (Wang & Law 2002), with the entrainment coefficient increasing steadily from jet-like (0.0528) to plume-like (0.0874) during the penetration (figure 17). For non-Boussinesq starting forced plumes, however, the entrainment behaviour was vastly different in the initial

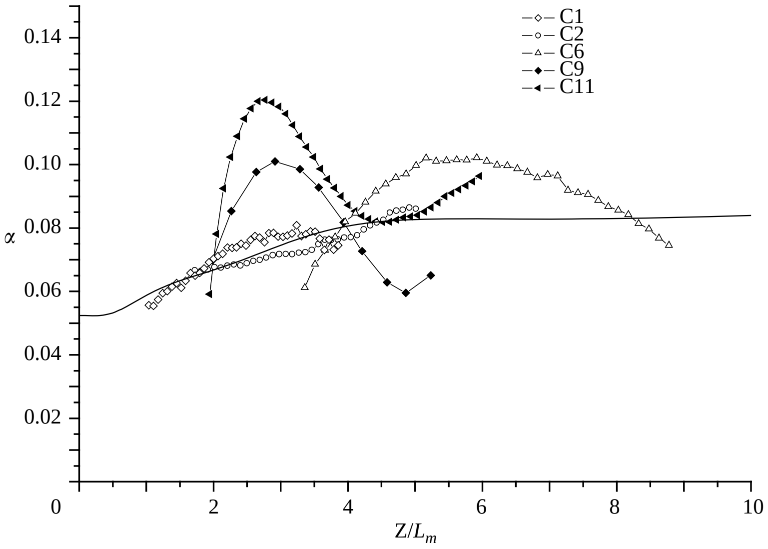

FIGURE 17. Variation of entrainment coefficient with Z/L_m. —, Wang & Law (2002).

region. Corresponding to the initial increase of the centreline velocity (see figure 11), there was a sharp increase initially for the entrainment coefficient and volume entrainment for both Cases C11 and C9. The entrainment coefficient jumped to a peak of 0.12 for Case C11 and 0.1 for Case C9. With the turbulent mixing, the plume fluid was rapidly diluted by the surrounding fluid and the behaviour finally achieved a self-preserving state as in the Boussinesq cases (see figures 10 and 17).

7. Temporal evolution of the velocity distribution

According to the penetration rate, the arrival time scale of the plume front should be $t \sim Z/L_m \times M_0/B_0$. In the following, we shall apply this time scale to estimate the transitional time for the centreline velocity evolution.

Figure 18 shows the variations of the dimensionless velocity versus the penetration time normalized with the above time scale. From the figure, it can be seen that the time scale accorded well with the present results and the normalized rising time T_r was around 0.5. After reaching a local peak owing to overshoot, the velocity began a periodic pulsation. The pulsation was stronger during the transition period and was attenuated slightly after the trailing stem became near steady state. The figure also shows that the centreline velocity fluctuation in the axial direction was about 0.3, which was close to the previous results reported in Shabbir & George (1994) and Wang & Law (2002) for steady forced plumes.

The typical Gaussian profile evolution with time is illustrated in figure 19. From the figure, the cross-sectional velocity profile was initially top-hatted when the plume front first arrived. An overshoot was recorded at $t = 2.8$ s. Subsequently, the centreline velocity oscillated around the mean value and the cross-sectional profile became Gaussian with the radius increasing monotonically towards the steady value. The Gaussian radius took much longer to attain a steady value than the centreline velocity.

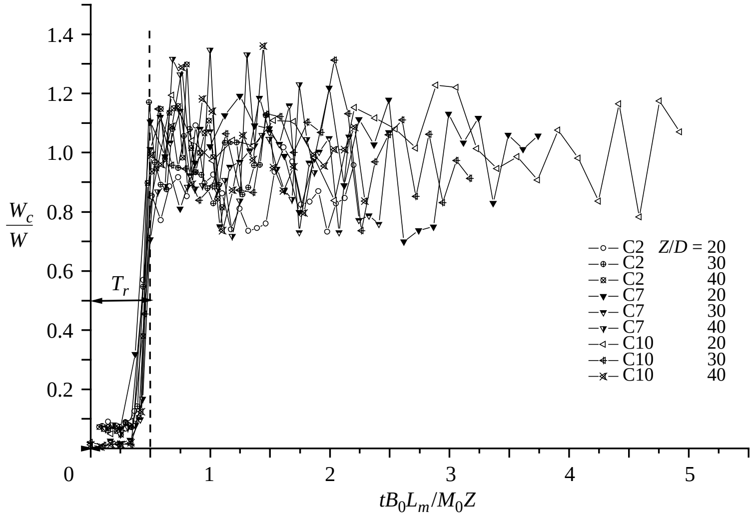

FIGURE 18. Time evolution of centreline velocity.

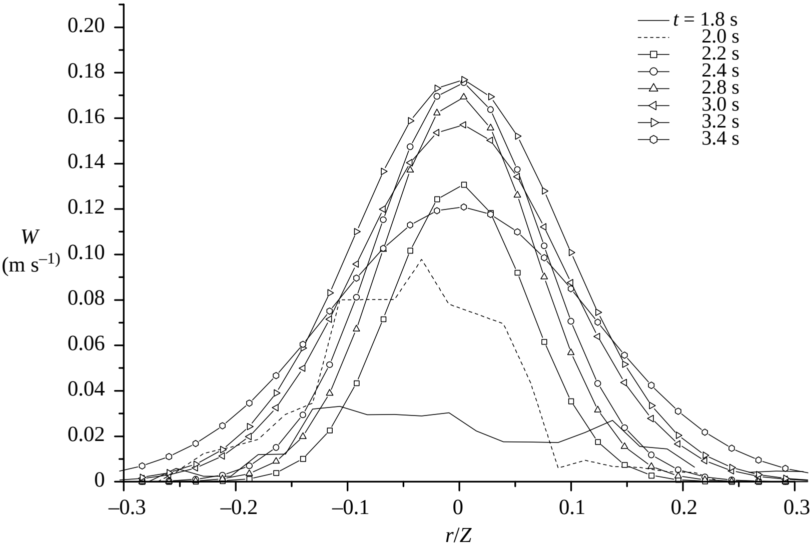

FIGURE 19. Time evolution of cross-sectional velocity at $Z/D = 30$ for Case C1.

8. Concluding remarks

Two distinct periods, the period of flow development and period of developed flow, are identified in the penetration behaviour of a starting forced plume. An analytical model is developed for the penetration rate in the period of developed flow by coupling the dynamics of the head vortex and the trailing forced plume. The unified model predicts the penetration rates in the three different phases of jet-like, transitional and plume-like behaviour in PDF, and computes directly the variations of the velocity ratios between the head vortex and the trailing forced plume.

Experiments were conducted on both Boussinesq and non-Boussinesq starting forced plumes using combined PIV and PLIF. For the Boussinesq cases, the measurements on the penetration rate agreed well with the model predictions. Other characteristics such as the radial penetration and entrainment rate also demonstrated reasonable agreement with previous results reported in the literature. For non-Boussinesq cases, flapping motion was observed to be more significant, and the temporal change in the centreline velocity had a strong overshoot in the initial region unlike the exponential decay observed in the Boussinesq cases. It was found that the non-Boussinesq effects near the source can be corrected by a virtual origin in the plume-like region similar to a non-Boussinesq steady forced plume.

A complete analytical model of the penetration of a starting forced plume requires the detailed simulation of the processes inside the PFD in addition to the PDF. Further work is obviously required in this area and is currently being pursued.

Scholarship support by the Nanyang Technological University for J.J.A. is gratefully acknowledged. The authors would also like to thanks the anonymous reviewers for their constructive comments.

Appendix

In this Appendix, we review some fundamental theory of the steady forced plume, which is essential to characterize its behaviour, and forms the basis of the presentation of the experimental results. The theory was first proposed by Morton *et al.* (1956).

The common assumption is that the profiles of mean velocity and density differences are Gaussian with length scales b_w and b_d, and maximum centreline values W_c and g'_c, respectively, all being functions of the height Z above a virtual origin. Thus, the cross-sectional variations of the mean axial velocity W and reduced gravity g' can be expressed as,

$$\frac{W}{W_c} = \exp^{-(r/b_w)^2}, \tag{A 1}$$

$$g' = g(\rho_\infty - \rho)/\rho_\infty = g'_c \exp^{-(r/b_d)^2}, \tag{A 2}$$

where ρ is the local density.

The volume flux, Q, can be obtained from the Gaussian velocity profile (equation (A1)) by integration as $\pi b_w^2 W_c$. Morton *et al.* (1956) proposed the entrainment principle, namely, that the rate of increase of volume flux per unit height is equal to $2\pi b_w \alpha W_c$, where α is the entrainment coefficient. The conservation equations over a particular cross-section can then be written as:

$$\mathrm{d}(b_w^2 W_c)/\mathrm{d}Z = 2\alpha b_w W_c, \tag{A 3}$$

$$\mathrm{d}(b_w^2 W_c^2)/\mathrm{d}Z = 2 b_d^2 g'_c, \tag{A 4}$$

$$\mathrm{d}B/\mathrm{d}Z = 0, \tag{A 5}$$

where the specific buoyancy flux, B, is

$$B = \frac{\pi b_w^2 b_d^2}{b_w^2 + b_d^2} W_c g'_c = B_0. \tag{A 6}$$

Assuming $b_w = b_d = b$, similarity solutions for b, W_c and g'_c were obtained by Morton *et al.* (1956)

$$b \propto Z, \quad W_c \propto B_0^{1/3} Z^{-1/3}, \quad g'_c \propto B_0^{2/3} Z^{-5/3}. \tag{A 7}$$

REFERENCES

Ai, J. J., Yu, S. C. M., Law, A. W. K. & Chua, L. P. 2005 Vortex dynamics in starting square water jets. *Phys. Fluids* **17**, 014106, 1–12.

Carlotti, P. & Hunt, G. R. 2005 Analytical solutions for turbulent non-Boussinesq plumes. *J. Fluid Mech.* **538**, 343–359.

Cossali, G. E., Coghe, A. & Araneo, L. 2001 Near-field entrainment in an impulsively started turbulent gas jet. *AIAA J.* **39**, 1113–1122.

Crow, S. C. & Champagne, F. H. 1971 Orderly structure in jet turbulence. *J. Fluid Mech.* **48**, 547–591.

Delichatsios, M. A. 1979 Time similarity analysis of unsteady buoyant plumes in neutral surroundings. *J. Fluid Mech.* **93**, 241–250.

Didden, M. 1979 On the formation of vortex rings: rolling-up and production of circulation. *Z. Angew. Math. Phys.* **30**, 101–116.

Diez, F. J., Sangras, R. & Faeth, G. M. 2003 Self-preserving properties of unsteady round buoyant turbulent plumes and thermals in still fluids. *Trans. ASME* C: *J. Heat Transfer* **125**, 821–830.

Fischer, H. B., List, E. J., Imberger, J. & Brooks, N. H. 1979 *Mixing in Inland and Coastal Waters.* Academic.

Gharib, M., Rambod, E. & Shariff, K. 1998 A universal time scale for vortex ring formation. *J. Fluid Mech.* **360**, 121–140.

Glezer, A. 1988 The formation of vortex rings. *Phys. Fluids* **31**, 3532–3542.

Helmholtz, H. 1858 On integrals of the hydrodynamical equations which express vortex-motion. Transl. P. G. Tait, 1867 with a letter by Lord Kelvin (W. Thomson), in *Lond. Edin. Dub. Phil. Mag. J. Sci.* Fourth series **33**, 485–512.

Heskestad, G. 1972 Similarity relations for the initial convective flow generated by fire. *FM Rep. 72-WA/HT-17,* Factory Mutual Research Corporation, Norwood, MA.

Hill, P. G. & Ouellette, P. 1999 Transient turbulent gaseous fuel jets for diesel engines. *Trans. ASME* I: *J. Fluids Engng* **121**, 93–100.

Johari, H., Zhang, Q. & Bourque, M. 1997 Impulsively started turbulent jets. *AIAA J.* **35**, 593–662.

Kelvin, Lord (Thomson, W.) 1880 Vibrations of a columnar vortex. *Lond. Edin. Dub. Phil. Mag. J. Sci.* Fifth series **10**, 155–168.

Lahbabi, F. Z., Boree, J. & Charnay, G. 1993 Analysis of starting and steady turbulent jets by image processing techniques. *ASME Third Symp. on Experimental and Numerical Flow Visualization FED172, New York*, pp. 315–321.

Lamb, H. 1932 *Hydrodynamics.* Cambridge University Press.

Law, A. W. K. & Wang, H. 2000 Measurements of mixing processes using combined DPIV and PLIF. *Exp. Thermal Fluid Sci.* **22**, 213–229.

Lim, T. T. & Nickels, T. B. 1995 Vortex rings. In *Fluid Vortices* (ed. S. I. Green), pp. 95–153. Kluwer.

List, E. J. 1982 Turbulent jets and plumes. *Annu. Rev. Fluid Mech.* **14**, 189–212.

Lundgren, T. S. & Mansour, N. N. 1991 Vortex ring bubbles. *J. Fluid Mech.* **224**, 523–529.

Maxworthy, T. 1977 Some experimental studies of vortex rings. *J. Fluid Mech.* **81**, 465–495.

Middleton, J. H. 1975 The asymptotic behaviour of a starting plume. *J. Fluid Mech.* **72**, 753–751.

Morton, B. R. 1959 Forced plumes. *J. Fluid Mech.* **5**, 151–163.

Morton, B. R., Taylor, G. I. & Turner, J. S. 1956 Turbulent gravitational convection from maintained and instantaneous sources. *Proc. R. Soc. Lond.* A **234**, 1–23.

Pantzlaff, L. & Lueptow, R. M. 1999 Transient positively and negatively buoyant turbulent round jets. *Exps. Fluids* **27**, 117–125.

Papanicolaou, P. N. & List, E. J. 1988 Investigations of round vertical turbulent buoyant jets. *J. Fluid Mech.* **195**, 341–391.

Papps, D. A. & Wood, I. R. 1997 The effect of an intermittent flapping motion on the properties of merging plumes. *J. Hydraul. Res.* **35**, 455–474.

Pullin, D. I. 1979 Vortex ring formation at tube and orifice openings. *Phys. Fluids* **22**, 401–403.

Ricou, F. P. & Spalding, D. B. 1961 Measurements of entrainment by axisymmetrical turbulent jets. *J. Fluid Mech.* **11**, 21–32.

Rooney, G. G. & Linden, P. F. 1996 Similarity considerations for non-Boussinesq plumes in an unstratified environment. *J. Fluid Mech.* **318**, 237–250.

Rooney, G. G. & Linden, P. F. 1997 Strongly buoyant plume similarity and ‘small-fire’ ventilation. *Fire Safety J.* **29**, 235–258.

Saffman, P. G. 1975 On the formation of vortex rings. *Stud. Appl. Maths* **54**, 261–268.

Saffman, P. G. 1978 The number of waves on unstable vortex rings. *J. Fluid Mech.* **84**, 625–639.

Sangras, R. & Faeth, G. M. 1999 Buoyant turbulent jets and plumes:III. Round turbulent nonbuoyant starting jets and puffs and buoyant starting plumes and thermals. *Annu. Rep. H.R. Baum, NIST Scientific Officer, Rep. No. GDL/GMF-99-03.*

Sangras, R., Kwon, O. C. & Faeth, G. M. 2003 Self-preserving properties of unsteady round nonbuoyant turbulent starting jets and puffs in still fluids. *Trans. ASME: J. Heat Transfer* **124**, 460–469.

Shabbir, A. & George, W. K. 1994 Experiments on a round turbulent buoyant plume. *J. Fluid Mech.* **275**, 1–32.

Shariff, K. & Leonard, A. 1992 Vortex rings. *Annu. Rev. Fluid Mech.* **24**, 235–279.

Turner, J. S. 1957 Buoyant vortex rings. *Proc. R. Soc. Lond.* A**239**, 61–75.

Turner, J. S. 1962 The ‘starting plume’ in neutral surroundings. *J. Fluid Mech.* **13**, 356–368.

Turner, J. S. 1969 Buoyant plumes and thermals. *Annu. Rev. Fluid Mech.* **1**, 28–44.

Wang, H. & Law, A. W. K. 2002 Second-order integral model for a round turbulent buoyant jet. *J. Fluid Mech.* **459**, 397–428.

Witze, P. O. 1980 The impulsively-started incompressible turbulent jet. *Sandia Natl Lab., Rep. SAND80-8617*, Livermore, CA, USA.

Woods, A. W. 1997 A note on non-Boussinesq plumes in an incompressible stratified environment. *J. Fluid Mech.* **345**, 347–356.

Wyganski, I. & Fiedler, H. 1969 Some measurements in the self-preserving jet. *J. Fluid Mech.* **38**, 577–612.

Zhou, X., Luo, K. H. & Williams, J. J. R. 2001 Study of density effects in turbulent buoyant jets using large-eddy simulation. *Theoret. Comput. Fluid Dyn.* **15**, 95–120.